



Water tank studies of atmospheric boundary layer structure and air pollution transport in upslope flow systems

C. Reuten,¹ D. G. Steyn,¹ and S. E. Allen¹

Received 2 October 2006; revised 2 February 2007; accepted 9 March 2007; published 13 June 2007.

[1] Heated mountain slopes sometimes vent air pollutants out of the boundary layer over the slope top and at other times trap pollutants in closed circulations. Field, numerical, and water tank studies of fair weather atmospheric conditions over complex terrain have shown more complicated vertical distributions of temperature, moisture, and aerosols than over horizontal terrain. To study these phenomena, we analyze flow fields, densities, and dye distributions in a bottom-heated salt-stratified water tank over a 19° slope with adjacent plain and plateau and compare with field and numerical model data. Vertical layering of dye results from upslope and plain-plateau circulations. The thermal boundary layer (TBL, the bottom layer up to neutral buoyancy height), coincides with the lower branches of these circulations. The return flow branches form elevated layers (EL) with properties intermediate between the TBL and environmental background. As heating continues, the TBL rapidly entrains the ELs, leading to deeper circulations with new ELs at greater heights. Field data suggest that successive formation and entrainment of ELs occurs at multiple scales in the atmosphere. If the aerosol loading of an EL is too high to distinguish it from the underlying TBL on lidar backscatter scans, then both layers and the associated closed circulation appear embedded in one deep backscatter boundary layer. The findings suggest defining the atmospheric boundary layer in complex terrain on the diurnal heating timescale rather than the commonly used 1-hour timescale, which is more appropriate for flat terrain. We discuss conditions leading to venting versus trapping of air pollutants.

Citation: Reuten, C., D. G. Steyn, and S. E. Allen (2007), Water tank studies of atmospheric boundary layer structure and air pollution transport in upslope flow systems, *J. Geophys. Res.*, 112, D11114, doi:10.1029/2006JD008045.

1. Introduction

[2] Thermally driven upslope flows play a critical role in the transport of heat and air pollution in complex terrain during fair weather conditions. Although they have been studied for over 160 years (see *Atkinson* [1981] for a review of the quantitative work until about 1980), basic questions concerning air pollution transport remain unanswered for different reasons. Field observations often suffer from sparse data and measurement uncertainties. Furthermore, land-use inhomogeneities, complicated topography, and larger-scale flows disturb and interact with upslope flows [*Banta*, 1984; *Wooldridge and McIntyre*, 1986; *Vergeiner and Dreiseitl*, 1987; *Vogel et al.*, 1987; *Kuwagata and Kondo*, 1989; *Blumen*, 1990; *Grønås and Sandvik*, 1999; *de Wekker*, 2002; *Rampanelli et al.*, 2004; *de Wekker et al.*, 2005; *Reuten et al.*, 2005]. Numerical mesoscale models, because of their limited horizontal resolution, are unlikely to reproduce the small scale of upslope flows in steep complex terrain. Large-eddy simulations (LES) are more promising

[*Revell et al.*, 1996; *Chow et al.*, 2006; *Weigel et al.*, 2006a, 2006b]. At horizontal resolutions of several hundred meters these models still contain most turbulent kinetic energy at the parameterized subgrid scale [*Weigel et al.*, 2006b], but they clearly resolve eddy structures on the scale of less than 1 km [*Colette et al.*, 2003]. *Schumann* [1990] ran an LES of an infinite slope under steady-state conditions producing results in good agreement with *Prandtl's* [1952] analytical solution. Analytical models and their numerical solution require restrictive assumptions and boundary conditions [*Egger*, 1981; *Petkovšek*, 1982; *Vergeiner*, 1982; *Kondo*, 1984; *Brehm*, 1986; *Segal et al.*, 1987; *Ye et al.*, 1987; *Haiden*, 1990, 2003; *Ingel'*, 2000]. Water tank models are limited by their simple topography, restricted by side and end walls, and their scaling poses an additional challenge. However, a carefully designed tank can be a good scale model of real topography and realistic atmospheric conditions. Tank experiments are highly repeatable [*Mitsumoto*, 1989] and permit measurements that are impossible in the field. Surprisingly few water tank studies of upslope flows have been carried out [*Deardorff and Willis*, 1987; *Mitsumoto*, 1989; *Chen et al.*, 1996; *Hunt et al.*, 2003]. None of these studies investigated the role upslope flows play in the transport of air pollutants, which will be the focus in this paper. Future tank studies could also benefit from substantial advances in experi-

¹Atmospheric Science Program, Department of Earth and Ocean Sciences, University of British Columbia, Vancouver, British Columbia, Canada.

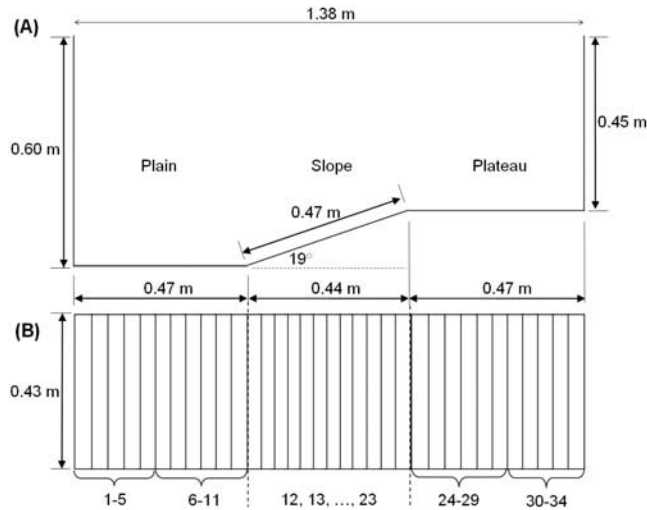


Figure 1. (a) Schematic side and (b) plan view of the water tank. In Figure 1b the strip heaters underneath the tank bottom are numbered from 1 to 34. Their heat output can be controlled individually underneath the slope and in two groups of five to six heaters each underneath plain and plateau as indicated.

mental techniques (*Moroni and Cenedese* [2006] and *Eck et al.* [2005] provide good examples in convection experiments).

[3] We designed a water tank scale model based on the nearly ideal conditions of field observations found in the work of *Reuten et al.* [2005]. The tank, field observations, and scaling are introduced in section 3. Experimental results with a particular emphasis on the transport of air pollutants are presented in section 4 and discussed in section 5. *Seibert et al.* [2000] define the term “atmospheric boundary layer” based on the dispersion of pollutants on a 1-hour timescale but emphasize that this definition possibly requires modifications in complex terrain regions. On the basis of the tank observations we suggest such a modification in the discussion section. Conclusions are drawn in section 6.

2. Methods

[4] We provide an overview of the water tank and measurement methods (section 3.1), the field observations

(section 3.3), and the scaling between water tank and atmosphere (section 3.4). *Reuten* [2006] and *Reuten et al.* [2005] contain additional details.

2.1. Water Tank

2.1.1. Design

[5] The water tank consists of a stainless steel frame enclosing glass walls and a stainless steel bottom with plain, 19° slope, and plateau (Figure 1). Convection is triggered in the tank with 34 strip heaters (Watlow Mica) underneath the bottom plate with a maximum total power of about 14 kW, which can be manually controlled individually or in groups of five to six heaters in a range from 30 to 100% of the total power. All water tank experiments covered in this manuscript were run with constant (in time) power supply, which resulted in steady bottom heat flux. We tested the steadiness by plotting specific volume versus time in a well-mixed nonstratified experiment and in a stratified experiment over the flat plateau with the rest of the tank separated by a removable wall. Good agreement with the expected specific volume development suggests that the heat gain is steady. A control experiment with approximately sinusoidally time varying bottom heat flux (as in the atmosphere) showed properties very similar to the experiments analyzed here. We conclude that using a steady heat flux is not a substantial constraint.

2.1.2. Background Stratification

[6] We will use the term “background stratification” for the initial stratification of the water in the tank and the air in the atmosphere to indicate the “background” environment into which the boundary layer grows. At the beginning of each experiment, the water was linearly salt stratified, which we achieved with a modification to the two-bucket method [*Fortuin*, 1960], described in Appendix A.

2.1.3. Overview of Experiments and Measurements

[7] We report results from two dye experiments, WT-Dye and HFD-Dye, and three particle experiments, WT-Part, SP-Part, and TR-Part (Table 1). In dye experiment WT-Dye (Whole Tank), the tank was heated uniformly. The experiment started with a submillimeter thin layer of fluorescent Uranine dye over the plain. A 2 cm wide and 30 cm tall light sheet illuminated the dye through the plain’s end wall. Convection from the heated tank bottom dispersed the dye, similar to air pollutants emitted by area sources into the atmosphere.

Table 1. Parameter Settings of Water Tank Experiments WT-Dye (Whole Tank Dye), WT-Part (Whole Tank Particle), SP-Part (Short Plain Particle), TR-Part (Triangular Ridge Particle), and HFD-Dye (Heat Flux Decrement Dye)

Parameter	WT-Dye	WT-Part	SP-Part	TR-Part	HFD-Dye
Particle (P) or Dye (D) experiment	D	P	P	P	D
Background buoyancy frequency, s^{-1}	0.379	0.379	0.379	0.342	0.567
Length of plain, m	0.470	0.470	0.225	0.470	0.470
Length of plateau, m	0.470	0.470	0.470	0	0.470
Heat flux over plain, $10^{-3} K m s^{-1}$	1.85	1.85	1.85	1.48/2.04 ^a	3 ^b
Heat flux over slope, $10^{-3} K m s^{-1}$	1.85	1.85	1.85	2.59–3.70 ^c	3/1–2 ^d
Heat flux over plateau, $10^{-3} K m s^{-1}$	1.85	1.85	1.85	-	3 ^b
Spatially average heat flux, $10^{-3} K m s^{-1}$	1.85	1.85	1.85	3.15	3 ^b

^aSurface heat flux was $1.48 \times 10^{-3} K m s^{-3}$ for heaters 1–5 and $2.04 \times 10^{-3} K m s^{-1}$ for heaters 6–11 (Figure 1).

^bIn this early experiment, uncertainties in heat flux were very high.

^cSurface heat flux increased in twelve equal increments from 1.67 to $3.70 \times 10^{-3} K m s^{-1}$ from slope base to ridge.

^dSurface heat flux was about $3 \times 10^{-3} K m s^{-3}$ in bottom two thirds of the slope and roughly $1-2 \times 10^{-3} K m s^{-1}$ in upper third.

[8] In dye experiment HFD-Dye (Heat Flux Decrement), which had lower heat flux on the upper slope, we dropped red-purple KMnO_4 crystals over the plateau near the right end wall (Figure 1), injected a column of green food coloring over the slope top, and released a plume of yellow food coloring at the slope base. This provided qualitative information about convection and horizontal motions at different locations in the tank.

[9] In particle experiments WT-Part (Whole Tank), SP-Part (Short Plain of 22.5 cm length), and TR-Part (Triangular Ridge; additional end wall at the slope top) we measured two-dimensional velocity fields from the motion of neutrally buoyant particles using Particle Image Velocimetry (PIV) programs for Matlab (MatPIV) developed by J. Kristian Sveen (www.math.uio.no/~jks/matpiv/). The particles were made from high-temperature wax (CALWAX 220) mixed at different ratios with titanium dioxide pigment, thus covering a range of densities. We mixed the particles into Kodak Professional Photo-Flo 200 to reduce surface tension, added the slurry at the water surface of the filled tank, and let the particles settle to their neutral buoyancy height. During the experiments, which lasted roughly 1000 s, the particles were illuminated as in WT-Dye. The observed velocity fields covered an area of approximately 40 cm width and 30 cm height. The motion of the particles was digitally recorded at a rate of 30 frames per second and the raw video was time lapsed by a factor of three. For PIV analyses, we got best results by comparing every second frame of the final video. The resulting velocity fields were therefore 0.2 s apart. We removed turbulent variations and data gaps by determining the median over 20-s intervals from 100 velocity fields. This duration is similar to the horizontal advection time for the upslope flow and the vertical convection time of rising thermals and roughly corresponds to 10 min in the atmosphere (see section 3.4 below). The uncertainty of the velocity measurements was approximately 20%.

[10] Specific volume is the inverse of density. It increases linearly with height in water with constant positive buoyancy frequency and therefore is comparable with potential temperature in the atmosphere. We determined vertical profiles of specific volume from the output of conductivity and temperature probes by Precision Measurement Engineering, Inc., which were driven up and down by a profiler. The manufacturer specifies a temperature accuracy of 0.05°C , a temperature time response of 7×10^{-3} s, and a time response of conductivity measurements of -3 db at approximately 800 Hz. Uncertainties in the calibration, measurement, and conversion procedure added to the roughly 2% accuracy of salt concentration measurements. The conductivity and temperature probes consist of sensors located at the bottom tip of vertically installed shafts. During upward motion, the shafts drag fluid from lower to greater heights (“selective withdrawal” [Turner, 1973]) so that the sensors at the bottom measure the conductivity and temperature of originally lower heights. During downward motion, the sensors take measurements of the surrounding fluid before the fluid height is altered. We therefore only took measurements during the descents and did not include the upward measurements that were under the influence of the withdrawn water. Measurements were started from a prescribed maximum height, which increased

during each experiment to account for the increasing depth of convection in the tank. When the profiler reached a height of 4 mm above the tank bottom, it returned to a new maximum height to start again. Profile depths increased from approximately 20 to 30 cm and profile acquisition increased from 13 to 20 s. Returning the probes to the top position and initialization created a 14–24 s gap between the profiles. The probes were driven downward while continuously acquiring data every 0.25 s at a vertical resolution of 3.5–4.0 mm. Each acquired datum consists of the mean of eight individual measurements. These specifications are roughly comparable to tethered sonde profiles 1000–1500 m deep, acquired over 10 min, with a sampling rate of 5 s, giving a vertical resolution of 20 m (see section 3.4 below for more details).

2.2. Methods for Determining the Boundary Layer Structure

[11] On the basis of *Seibert et al.* [2000] it can be expected that different methods of determining the boundary layer structure will lead to different results. Over flat homogeneous terrain during daytime and fair weather conditions, *Seibert et al.* [2000] report differences of approximately 10%. This is roughly equal to the uncertainty of the field data in the work of *Reuten et al.* [2005] and the tank data reported here and will not be subject of this study. In this communication, we will focus on much larger difference that can be attributed to particular flow structures over the slope. We use two terms for the atmospheric boundary layer based on two different measurement methods: “backscatter boundary layer” (BBL) and “thermal boundary layer” (TBL).

[12] *Strawbridge and Snyder* [2004] describe an algorithm, which was used by *Reuten et al.* [2005] to determine the BBL depth in the atmosphere with a Doppler lidar based on the strength of the vertical gradient of aerosol concentration in the atmosphere. In the water tank we applied the same method manually. During the experiments, the dye originally released over the tank bottom forms a strongly fluorescent BBL, which was captured every 10 s with a digital still camera and continuously with a digital camcorder. Overshooting thermals of dye-rich water against an essentially black background form a sharp boundary that can be identified with an uncertainty of one pixel corresponding to 0.2–0.3 mm in the vertical. During times of deep entrainment of clear water down into the BBL, the boundary becomes diffuse and the uncertainty increases to several millimeters. This method provides information on the average height of the BBL and the bottom and top of the entrainment layer, thus avoiding the problem of overestimating the BBL [*Seibert et al.*, 2000].

[13] The “thermal boundary layer” (TBL) is determined from thermal information. For the field data in the work of *Reuten et al.* [2005], tethered sonde measurements of temperature and humidity and surface measurements of temperature were combined to estimate the centre height of the entrainment zone using a simple parcel method [*Seibert et al.*, 2000]. We used a variation on the parcel method in the water tank based on profiles of specific volume. Because of a lack of measurements very near the tank bottom, we determined the top of the TBL as the centre height of the

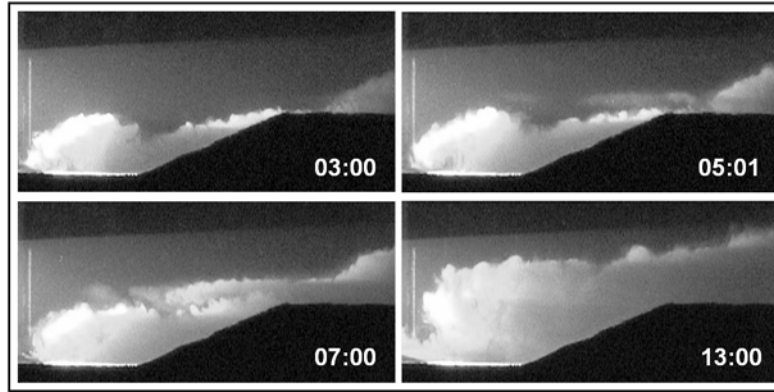


Figure 2. Movie frames of WT-Dye at the four times (in minutes and seconds) marked by the vertical dashed lines in Figure 3. The dye (Uranine) was originally released as a submillimeter thin layer over the entire plain and is illuminated from the left by a 2 cm wide and 30 cm tall light sheet. (The complete movie file is available as dynamic content).

stably stratified entrainment zone, which was mostly fairly shallow.

2.3. Field Observations

[14] The water tank is a model of an approximately homogeneous 3-km wide 19° slope with a ridge height of 760 m at Minnekhada Park in the Lower Fraser Valley, British Columbia, Canada [Reuten *et al.*, 2005, Figure 2]. During the day, aerosols are released mainly by area sources at the bottom of the Lower Fraser Valley and dispersed by convective heating. The process is comparable to the dispersion of Uranine dye in tank experiment WT-Dye. We therefore will use the term BBL for both the tank's dye layer and the atmosphere's aerosol layer. Range-height indicator (RHI) scans with a lidar provided information on the BBL depth over plain and slope. Our comparisons between tank and field observations will be limited to the morning hours of 25 and 26 July 2001, when synoptic winds were weak (about 2.5ms^{-1} at 850 hPa) and sea breeze and up-valley flows were not yet developed so that upslope flows were the main transport mechanism [Reuten

et al., 2005]. We focus on tank experiments of a particular “test case,” which was designed to model field conditions at 1100 PST (Pacific Standard Time, within 15 min of local solar time) on 25 July 2001 (Table 2).

2.4. Scaling

[15] The details of the scaling are beyond the scope of this communication and will be reported elsewhere but are discussed extensively in chapter 4 and section B.6 in the work of Reuten *et al.*, [2005]. Table 1 and Table 2 provide typical values, which can be used for comparison with other physical scale models. We emphasize that the appropriate definition and critical value of the Reynolds number, for example, require careful consideration, which are not elaborated here.

[16] We identified twelve key parameters. Six of these are critical for achieving similarity of bulk flow features in tank and atmosphere: the height of the slope, H in units of m, instantaneous kinematic heat flux Q_H in K m s^{-1} , buoyancy frequency N in s^{-1} , the horizontal length of the slope L in m, the kinematic energy density (total energy supplied

Table 2. Parameter Settings and Observations for Test Case

Parameter	Atmosphere ^a	Water Tank ^b
Time since positive heat flux t_{ref} , s	14, 400	300
Ridge height h , m	760	0.15
Horizontal length of slope L , m	2200	0.43
Background buoyancy frequency N , s^{-1}	0.015 ± 0.001	0.38 ± 0.02
Heat flux Q_H , K m s^{-1}	0.21 ± 0.05	$(1.9 \pm 0.2) \times 10^{-3}$
Integrated heat flux E , K m	1600×400	0.56×0.05
TBL depth h , m	720×120	0.14×0.02
Upslope flow velocity U , m s^{-1}	3.8×0.5	0.005×0.001
Convective velocity $w_* = (g\beta h Q_H)^{1/3}$, m s^{-1}	1.8	0.0087
Horizontal advection time $t_h = L/U$, s	630	25
Vertical convection time $t_v = h/w_*$, s	410	16
Reynolds number ^c $Re = hU/\nu$	1.7×10^8	2700
Rayleigh number ^d $Ra = g\Delta_s h^3/\kappa\nu$	1.9×10^{17}	4.4×10^8

^aAtmospheric data are for the field site at Minnekhada Park at 1100 PST 25 July 2001. All uncertainties in this table roughly represent 95% confidence intervals.

^bWater-tank data are for WT-Dye and WT-Part at 05:01.

^cHere ν is molecular viscosity.

^dHere κ is molecular diffusivity of heat; Δ_s is $\beta\Delta\theta$ in the atmosphere and $\Delta\alpha/\alpha_0$ in the tank, with β coefficient of thermal expansion, θ potential temperature, and α specific volume, where subscript “0” denotes initial surface values and Δ indicates increases from initial surface values.

Table 3. Similarity of Water Tank Experiments WT-Dye and WT-Part with the Atmosphere at Different Times

Water Tank Time, min:s ^c	Atmosphere ^a		ND Gov. Para. ^b			Name
	Time, PST ^d	N, s ⁻¹ ^e	Π_1	Π_2	Π_3	
03:00	0945	0.0134	2.9	68	0.0039	Midmorning
05:01	1100	0.0149	2.9	114	0.0039	Late morning (test case)
07:00	1205	0.0158 ^f	2.9	159	0.0039	Beginning afternoon
13:00	1445	0.0166	2.9	295	0.0039	Time of maximum heating

^aFor sinusoidally time-dependent heat flux where positive heat flux begins at 0700 PST and a maximum value of 0.289 K m s⁻¹ is reached at 1445 PST.

^bNondimensional governing parameters; tank and atmospheric values are equal.

^cTime (min:s) since the beginning of positive heat flux into the tank. For parameter settings see Table 1.

^dDetermined from (9).

^eBackground buoyancy frequency. Determined from (8).

^fRoughly corresponds to atmospheric conditions at the field site at 1205 PST 26 July 2001.

through the surface per unit area, determined as the time integral of Q_H since the beginning of positive heat flux) E in K m, and the buoyancy parameter $g\beta$ in m s⁻² K⁻¹ where g is the gravitational acceleration and β the coefficient of thermal expansion. There are three fundamental units, temperature (K), length (m), and time (s). According to the Buckingham Pi Theorem [Buckingham, 1914], three independent key parameters are needed to form three nondimensional governing parameters (Pi groups). A suitable choice of independent key parameters are the first three, H , Q_H , and N . The three Pi groups are then determined by appropriately nondimensionalizing the remaining three independent parameters. Nondimensionalized horizontal slope length is the aspect ratio

$$\Pi_1 = \frac{L}{H}, \quad (1)$$

By tank design, Π_1 is equal in tank and atmosphere. Nondimensionalizing energy density gives

$$\Pi_2 = E \cdot \frac{N}{Q_H}. \quad (2)$$

The third governing parameter is defined by nondimensionalizing the buoyancy parameter,

$$\Pi_3 = g\beta \cdot \frac{Q_H}{H^2 N^3}. \quad (3)$$

Instantaneous heat flux and total supplied energy are the direct physical drivers of the flows in tank and atmosphere. It is therefore more appropriate to refer to Π_3 as nondimensional heat flux.

[17] In the water tank, surface heat flux Q_H is steady so that $E = Q_H \cdot t$ and

$$\Pi_{2,w} = N_w \cdot t_w \quad (4)$$

is essentially a nondimensional time. The subscript “w” indicates that this equation only holds for the water tank. The expression for the atmosphere is far more complicated. We assume sinusoidally time-varying surface heat flux,

$$Q_{H,a}(t_a) = Q_{\max,a} \cdot \sin\left(\frac{\pi}{2} \frac{t_a}{t_{d,a}}\right), \quad (5)$$

where the subscript “a” emphasizes that this equation applies to the atmosphere only. In (5), $t_{d,a} \approx 7.75$ hours = 27,900 s is a diurnal heating timescale such that when positive heat flux begins at about 0700 PST, the maximum value of $Q_{\max,a} = 0.289$ K m s⁻¹ is reached at 1445 PST. With (5), the kinematic energy density for the atmosphere is

$$E_a = \int_0^{t_a} Q_{H,a}(t) dt = Q_{\max,a} t_{d,a} \cdot \frac{2}{\pi} \left[1 - \cos\left(\frac{\pi}{2} \frac{t_a}{t_{d,a}}\right) \right] \quad (6)$$

and (2) becomes

$$\Pi_{2,a} = t_{d,a} N_a \cdot \frac{2}{\pi} \left[1 - \cos\left(\frac{\pi}{2} \frac{t_a}{t_{d,a}}\right) \right] / \sin\left(\frac{\pi}{2} \frac{t_a}{t_{d,a}}\right). \quad (7)$$

This expression is complex and depends on the specific time development of heating in the atmosphere. Furthermore, it is not time but rather energy density that is the physical cause of the flow. We therefore prefer to call Π_2 “nondimensional energy density.”

[18] When tank and atmospheric values of Π_2 and Π_3 are matched (the aspect ratio Π_1 is matched by design of the tank), lidar scans and tank images agree qualitatively (section 5.1). The time of similarity between water tank and atmosphere can be determined as follows. $\Pi_{3,w}$ is constant. With (5) the requirement $\Pi_{3,a} = \Pi_{3,w}$ leads to a relationship between buoyancy frequencies N_w and N_a in water tank and atmosphere, respectively,

$$N_w(t_{a,sim}) = N_a \left[\frac{\beta_a}{\beta_w} \frac{H_w^2}{H_a^2} \frac{Q_{\max,a}}{Q_{H,w}} \sin\left(\frac{\pi}{2} \frac{t_{a,sim}}{t_{d,a}}\right) \right]^{-1/3} \quad (8)$$

where $t_{a,sim}$ denotes the atmospheric reference time of similarity with a particular water-tank experiment with given $Q_{H,w}$. With field observations of $Q_{\max,a}$, $t_{d,a}$, and N_a , all quantities on the right-hand side of (8) are known. Hence the buoyancy frequency required for the experiment, N_w , is fully determined by the choice of $t_{a,sim}$. This value needs to be chosen before the experiment. To achieve similarity for another instant in time on the same day in the atmosphere, another experiment with another N_w needs to be carried out. The time of similarity in the water tank $t_{w,sim}$ corresponding

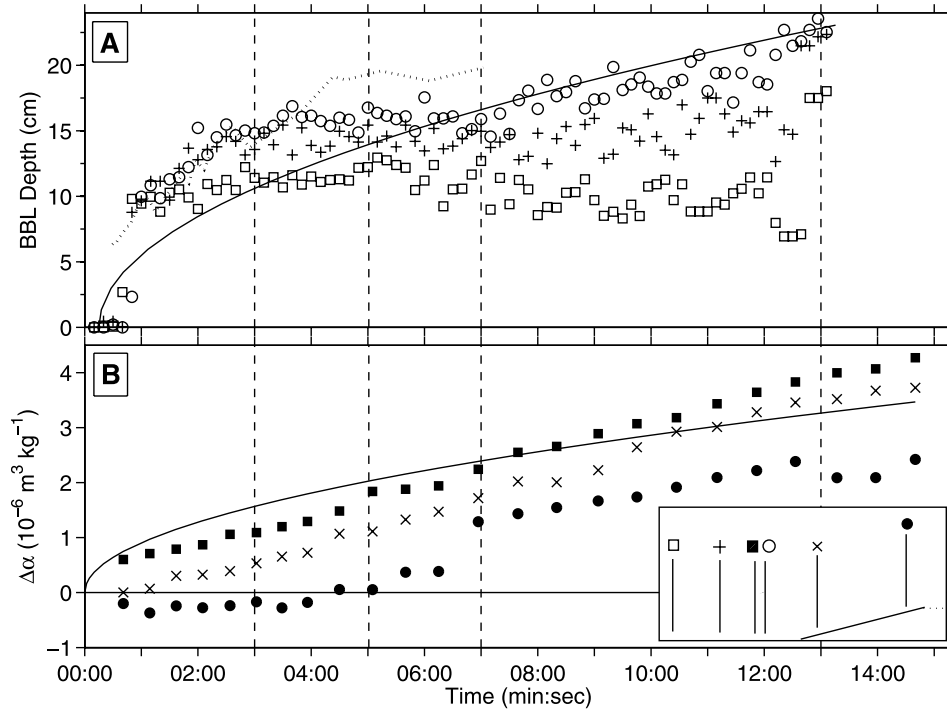


Figure 3. (a) Time development of backscatter boundary layer (BBL) depth (from WT-Dye) and (b) mean specific-volume increment $\Delta\alpha$ (from WT-Part). The latter is the difference between average specific volume within the thermal boundary layer (TBL) and the original surface value at that location. The inset in Figure 3b shows the locations of the measurements. The two solid curves are predictions from an encroachment model of TBL growth over a horizontal surface. The dashed vertical lines mark the times of the still images in Figure 2 and velocity fields in Figure 4. The dotted line in Figure 3a is based on lidar backscatter scans over the plain near the slope base at Minnehkaha Park in the morning of 25 July 2001. For the conversion from atmospheric time and BBL depth to laboratory time and BBL depth, see Reuten [2006].

to $t_{a,sim}$ can be derived by substituting (4) and (7) into the similarity requirement $\Pi_{2,a} = \Pi_{2,w}$ and solving for t_w ,

$$t_{w,sim} = \frac{N_a}{N_w(t_{a,sim})} \cdot t_{d,a} \cdot \frac{2}{\pi} \left[1 - \cos\left(\frac{\pi t_{a,sim}}{2 t_{d,a}}\right) \right] \cdot \left[\sin\left(\frac{\pi t_{a,sim}}{2 t_{d,a}}\right) \right]^{-1} \quad (9)$$

where the notation $N_w(t_{a,sim})$ emphasizes that N_w must be determined through (8) as a function of $t_{a,sim}$.

[19] An important corollary of the last two equations is: The same experiment with initial background buoyancy frequency N_w can be used to check similarity with atmospheric observations on different field days with different background buoyancy frequencies N_a . Table 3 shows that the tank experiments WT-Dye and WT-Part represent realistic atmospheric scenarios over a long period, including the test case at 05:01 (min:s, time elapsed after start of heat flux into the tank).

3. Results

3.1. Flow Characteristics, Layering, and Regime Changes

[20] We will show that mean characteristics of the water-tank flow remain unchanged for considerable periods. “Regime changes” of the flow geometry are associated with substantial changes in velocity and specific-volume

distribution. In this section, we will analyze the whole-tank experiments WT-Dye and WT-Part (Table 1) at four tank times, 03:00, 05:01, 07:00, and 13:00. Corresponding atmospheric conditions were calculated with (8) and (9) and are shown in Table 3.

3.1.1. “Midmorning”: 03:00

[21] This early time in WT-Dye and WT-Part is similar to 1045 PDT (“midmorning”) in the atmosphere for a constant background buoyancy frequency of 0.0134 s^{-1} (Table 3), i.e., Π_2 and Π_3 in (2) and (3) are equal for tank and atmosphere. The predominant features at 03:00 in WT-Dye are a BBL bulge over the plain near the slope and BBL depressions at the end wall and over the lowest 10 cm of the slope (Figure 2). Over the plain, the BBL is 30–40% deeper than predicted by an encroachment model of TBL growth over a horizontal surface [Carson, 1973], while it agrees with the prediction near the left end wall (Figure 3). Notice that a much deeper BBL than predicted was also observed in the field (dotted line in A) at a location roughly corresponding to the location of the open circles 13 cm from the slope base (inset in B). See Reuten [2006, Figure 4.3] for more details on the comparison between field and tank data.

[22] The BBL distribution over the plain is caused by a clockwise (CW) rotating eddy near the slope base (Figure 4) and a counter clockwise (CCW) rotating eddy near the left end wall (see dynamic content). A net flow from the CCW

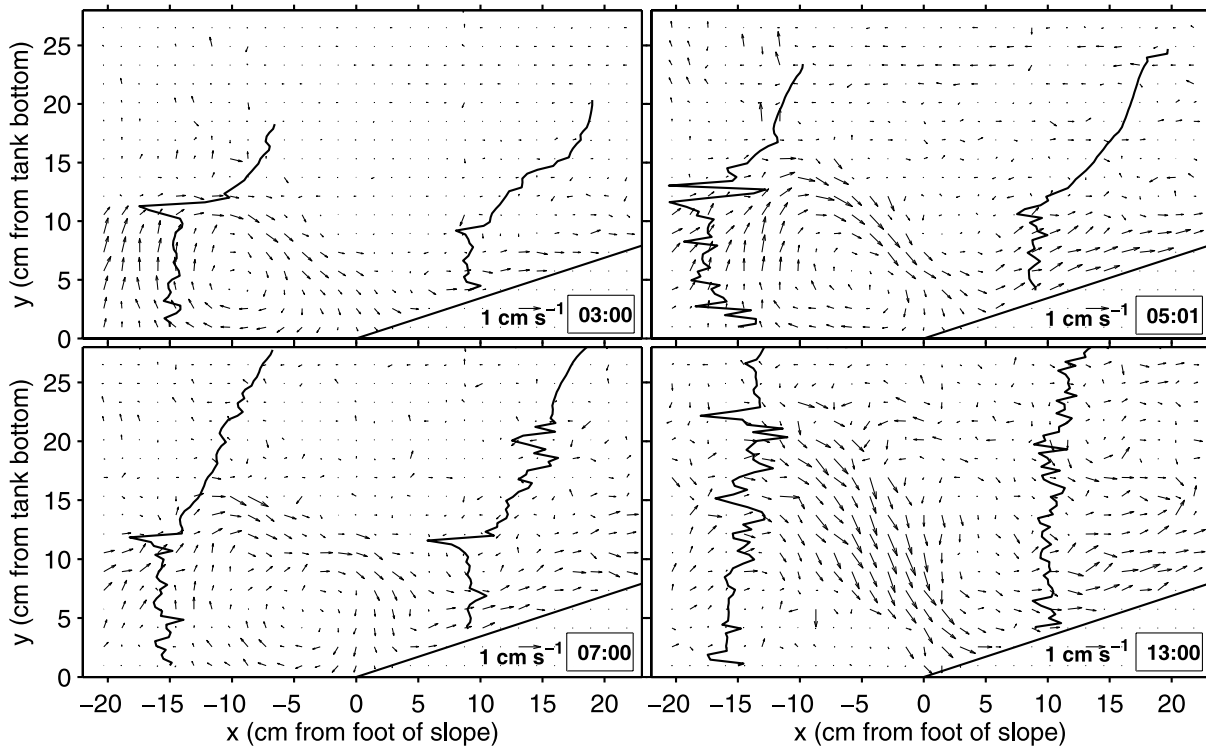


Figure 4. Two-dimensional velocity fields for WT-Part corresponding to the four still images in Figure 2 at the four times marked by vertical dashed lines in Figure 3. Fields are time medians over 20 s (100 individual fields) approximately centered at the indicated times of each graph. The solid curves are vertical profiles of specific volume (in arbitrary units) measured approximately during the averaging period of the velocity fields $x = -15$ cm to the left and $x = 9$ cm to the right of the slope base (at $x = 0$ cm). All length and velocity scales are identical in the four graphs. A representative velocity vector of length 1 cm s^{-1} is shown near the bottom right of each graph underneath the straight line indicating the slope surface. The sharp spikes in some profiles are probably caused by double diffusion and not a major factor for the overall flow but helpful indicators of layer boundaries.

rotating eddy into the CW rotating eddy leads to compensating subsidence near the left end wall and a deep BBL over the CW rotating eddy at about $x = -11$ cm (Figure 5). At $x = -15$ cm, TBL and BBL are about 11 cm deep. The downflowing part of the CW rotating eddy splits into a branch joining the upslope flow and a branch closing the eddy, the latter causing a flow in the downslope direction over the plain near the slope. *Mitsumoto* [1989] also observed the downslope flow, which persisted through complete cycles of diurnal heating and cooling and was independent of the length of the plain.

[23] From the BBL depression near the slope base to the top, BBL depth and upslope flow depth decrease approximately linearly to almost zero at the top (Figure 2 and dynamic content). Over the slope at $x = 9$ cm both TBL and BBL are only about 6 cm deep. On Figure 4 the upslope flow appears shallower than the TBL, but at this early stage, only a few particles are visible at greater heights, and data coverage is insufficient to determine upslope flow depth. Decreasing TBL depth with distance up the slope is corroborated by mean specific volume increments at 03:00 (Figure 3b), which are lower than expected over a horizontal surface. The slope is a transient region, where the upslope flow advects fluid with low specific volume into higher regions. Because strongest upslope velocity occurs

near the slope's midpoint ($0.5\text{--}0.6 \text{ cm s}^{-1}$ at about $x = 20$ cm, Figure 4), fluid parcels overshoot near the ridge causing negative specific volume increments. Near the slope base, specific volume in the TBL is slightly lower than expected.

[24] Decreasing upslope flow depth and velocity from slope midpoint to ridge imply decreasing mass flux and therefore compensating detrainment of fluid from the upslope flow. If the upslope flow fills the entire TBL such a detrainment has to occur vertically against gravity, because fluid from the upslope flow layer has a lower specific volume than the stratified fluid above, or laterally, adding a substantial three-dimensional (3-D) component to the overall flow. The video (dynamic content, animation 2) supports the former process and shows no evidence for the latter process at 03:00. The detrained fluid subsides over the lower part of the slope causing the BBL depression.

[25] At the slope top, a shallow plain-plateau flow transports dye toward the plateau's end wall, where it overshoots and returns the dye above the plain-plateau flow (Figure 2). The flow in the tank is very similar to the flow in an idealized infinite series of valleys between plateaus, where valley bottom and plateau half-widths equal the tank's plain and plateau lengths, respectively (Figure 6). A main difference is that velocities and turbulence at the tank walls must be zero unlike in an infinite repetitive domain. Furthermore,

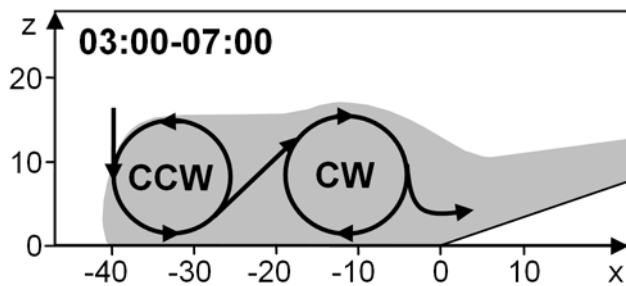


Figure 5. Schematic of eddies over the plain in WT-Dye and WT-Part from 03:00 to 07:00. “CW” and “CCW” denote the clockwise and counterclockwise rotating eddies, respectively. The grey region represents the BBL.

in the real atmosphere both geometry and solar radiation are not perfectly symmetric, permitting cross-flows and circulations at scales larger than those in the tank. However, since we observe strong vertical motions near the end wall, we expect the motions in the tank to be a reasonable qualitative representation of sufficiently symmetric atmospheric environments. In such atmospheric environments, the flow would initially be perceived as venting of aerosols over the slope top, but by joining the plain-plateau flow circulation, the dye returns above a growing TBL, which eventually reentrains the dye if heating continues.

3.1.2. “Late Morning” (“Test Case”): 05:01

[26] This is the time of expected similarity of WT-Dye and WT-Part with the atmosphere at 1100 PST 25 July 2001 (Table 2 and Table 3). Qualitatively, the flow characteristics remain unchanged from 03:00 to 05:01 (Figure 2 and Figure 4).

[27] The average depth of the BBL at the three locations over the plain in Figure 3a agrees with the value expected over a horizontal surface. From 03:00 to 05:01, the BBL depression has weakened (Figure 2). The CW rotating eddy has moved roughly 3 cm closer to the slope and the eddy’s velocity has slightly increased (Figure 4). At $x = -20$ cm, the flow from the CCW rotating eddy into the CW rotating eddy (as sketched in Figure 5) is clearly visible. At $x = -15$ cm, TBL and BBL are about 16 cm deep, and at $x = 9$ cm, TBL, BBL, upslope flow are about 8 cm deep. As before at 03:00, the BBL depth over the slope decreases approximately linearly to almost zero at the slope top. Between $x = 0$ and 5 cm, however, the upslope flow depth is only about 7 cm while the BBL is almost twice as deep. In the BBL above the upslope flow, velocities are weak with some return flow. Apparently, dye has been detrained from the upslope flow in the upper part of the slope and carried into the subsiding flow in the lower part, where it partly filled the BBL depression. The shallow plain-plateau flow is visible in Figure 4 between $y = 16$ and 19 cm and its return flow between $y = 22$ and 25 cm, which can be seen in Figure 2 as dye that has propagated horizontally from the plateau to above the midpoint of the slope.

3.1.3. “Beginning Afternoon”: 07:00

[28] At 07:00, WT-Dye and WT-Part model atmospheric conditions at 1205 PST with a background buoyancy frequency of 0.0158 s^{-1} , hence more stable than on 25 July, but slightly less stable than on 26 July (Table 3). Flow characteristics begin to change.

[29] The BBL depth over the plain has slightly decreased since 05:01 and has dropped below the value expected over a horizontal surface (Figure 3a). This is in line with a decrease of the TBL depth to roughly 13 cm at $x = -15$ cm (Figure 4). After 07:00, the BBL deepens again over the plain except near the end-wall (Figure 3a). Specific volume has continued to increase approximately linearly in time over the plain and near the slope base but has increased rapidly over the slope near the top (Figure 3b). The corresponding specific volume profiles (Figure 7, top) begin to exhibit a three-layer structure at 04:22–04:39: an unstable lower layer, a weakly stable middle layer, and a stable top layer (the initial background). The lower layer and the middle layer are separated by a sharp spike at about ridge height ($y = 15$ cm) probably caused by double diffusion [Reuten, 2006]. At 06:47–07:07, the lower layer and the middle layer, that is the upslope and the plain-plateau flow system, begin to merge. At the same time over the lower part of the slope at $x = 9$ cm (middle) and over the plain at $x = -15$ cm (bottom), a similar three-layer structure is just beginning to develop. At these two locations, the two lower layers merge later than over the slope near the top (not shown in Figure 7), although the plain-plateau flow system has disappeared already at 07:00 (Figure 4).

[30] Over the plain, TBL and BBL essentially agree. The top of the BBL at $x = -15$ cm (horizontal bars in Figure 7, determined from dynamic content) is systematically slightly higher than the TBL at $x = -13$ cm only because of the difference in location. At 06:47–07:07, the TBL top was slightly higher over the plain (bottom) than over the slope (middle), in agreement with the BBL top (Figure 2). The BBL depression over the slope and the bulge over the plain have almost disappeared, but the velocity field (Figure 4) still shows a bulge at about $x = -10$ cm and a deep depression between $x = 5$ and 10 cm. At this stage of the experiment, the dye has been substantially distributed throughout the tank, and inferences on instantaneous flow field and thermal structure from the BBL characteristics are more difficult than at earlier times.

3.1.4. “Time of Maximum Heating”: 13:00

[31] At 13:00, the water tank experiment is similar to atmospheric conditions at 1445 PST, with a background buoyancy frequency of 0.0166 s^{-1} , which is slightly higher than on 26 July (Table 3). The flow characteristics have changed substantially from those at 07:00.

[32] At $x = -13$ cm, the BBL depth has been growing as expected over a horizontal surface (Figure 3a). By comparison, at $x = -23$ cm and -33 cm it increased slowly until just before 13:00 when it increased rapidly to or near the expected value because the subsidence region near the

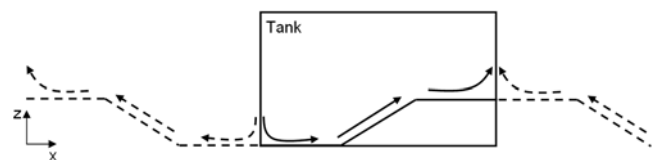


Figure 6. Mirror symmetry of water tank. The flow in the water tank (solid lines and arrows) models perfectly symmetric flow in an infinite array of valleys and plateaus as indicated by the dashed lines and arrows.

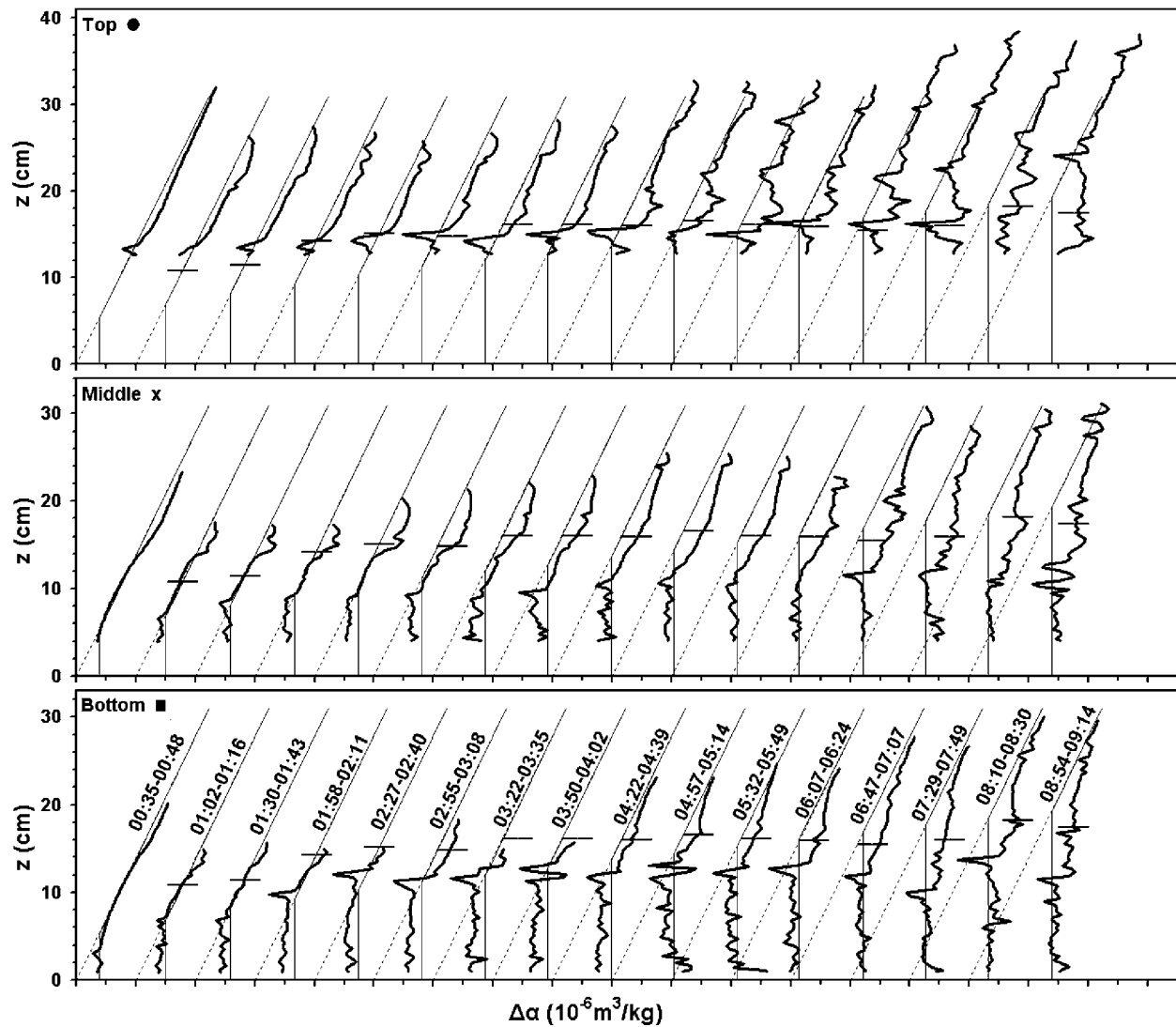


Figure 7. Vertical specific-volume profiles in WT-Part. The three graphs correspond to the locations in Figure 3b: $x = -15$ cm (bottom, square), $x = 9$ cm (middle, cross), and $x = 34$ cm (top, circle). The difference between tick marks on the x axis is $10^{-6} \text{ m}^3 \text{ kg}^{-1}$. The profiles are horizontally offset by $2 \times 10^{-6} \text{ m}^3 \text{ kg}^{-1}$ to avoid overlap. The times of measurement in minutes and seconds after the beginning of positive heat flux, shown only in the bottom graph, apply to the corresponding profiles in the other two graphs. Each profile is accompanied by the predicted specific volume profile (solid thin lines), the predicted initial background specific volume profile (dashed thin lines), and the BBL depth averaged over the time interval of the specific volume profiles (short horizontal bars), all relative to the plain. Specific volume is shown as the difference from the expected initial surface value over the plain.

plain's end wall narrowed, and at these two locations subsidence was replaced by deep convection. Specific volume at all three locations in Figure 3b has continued to increase approximately linearly in time and at 13:00 slightly exceeds the expected values over the plain and over the lower part of the slope. The average of the specific volume over the three locations agrees with the expected value over a horizontal surface. Over the upper part of the slope, specific volume remains much smaller, indicating that upslope flows continue advecting fluid of lower specific volume into the upper slope region. The top of the BBL slopes approximately linearly from near the plain's end wall to the plateau's end wall (Figure 2) at an aspect

ratio and angle of about one third of the bottom slope angle (6° – 7°). This agrees with *Deardorff and Willis* [1987], who also observed a sloping mixed layer top intermediate between horizontal and bottom slope angle.

[33] The two lowest layers at $x = 9$ cm (Figure 7, middle) and $x = -15$ cm (bottom), which have begun merging at 06:47–07:07, have formed a deep well-mixed TBL (about 23 cm at $x = 9$ cm and 26 cm at $x = -15$ cm, Figure 4), which agrees with the BBL (Figure 2). The CW rotating eddy is approximately 16 cm deep with its downward velocities exceeding 1 cm s^{-1} , but its lower flow in the downslope direction has disappeared (Figure 4). The upslope flow is strong (about 1 cm s^{-1}), shows no return

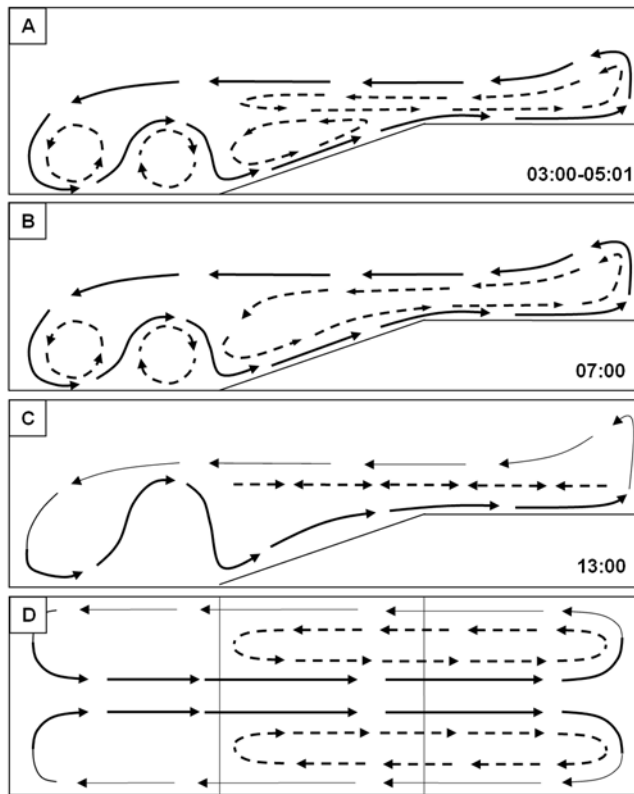


Figure 8. Sketches of flow characteristics in WT-Dye and WT-Part (a) between 03:00 and 05:01 and (b) at 07:00; dashed arrows denote small persistent circulations; solid arrows denote a large circulation, which appears superimposed on top of the smaller circulations. (c) Side view of flow characteristics at 13:00 and (d) plan view of C; flows to the right are partly compensated near the lateral side walls and partly at greater heights.

flow, and is shallower (10–15 cm) than TBL and BBL. The dynamic content, animation 2 reveals that the upslope flow in the center of the tank is partially compensated by a return flow near the side walls; (Figure 4 does not show this motion because particles near the side walls were out of focus and not illuminated and therefore automatically filtered in MatPIV). At the beginning of an experiment, heat conduction into the tank bottom is slow and dominated by molecular diffusion. Because the heat conductivity of stainless steel is much greater than that of water, the tank bottom is nearly homogeneously heated. As the flow becomes more turbulent, heat is transported faster into the water than along the stainless steel bottom, and less heat is supplied to water near the side walls. Because the entire flow in upslope direction cannot be compensated within the weakly heated narrow strip near the side wall, some of the flow moves against gravity at the right end-wall and returns above the plain-plateau flow. When lateral flows occur late in the experiment, the tank may no longer be a good model of the atmosphere.

3.1.5. Summary

[34] The merging of layers approximately at 07:00 and 13:00 in the vertical specific volume profiles corresponds to

flow regime changes. Flow characteristics at 03:00 and 05:01 were very similar. CCW and CW rotating eddies occurred over the plain (Figure 5), an upslope flow circulation over the slope, and a plain-plateau circulation over the slope and plateau. A large circulation filling the entire tank width was superimposed on top of the smaller circulations (Figure 8a).

[35] At 07:00, the upper part of upslope flow circulation and the bottom part of plain-plateau circulation merged and became one large circulation reaching from slope base to right end wall (Figure 8b). Just before 13:00, the eddies over the plain had disappeared and a large combined upslope and plain-plateau flow circulation deeper than ridge height occurred within a deep BBL (Figure 8c). Flows in upslope direction were partially compensated laterally near the side walls (Figure 8d).

3.2. Thermal Boundary Layer over Valley Centers

[36] Subsidence observed at the plain's end wall in WT-Dye (corresponding to the valley center of an infinite series of valleys between plateaus) agrees with the widely accepted notion that upslope flows over valley side walls cause compensating subsidence over the valley center [Whiteman, 2000]. In the tank it is plausible that subsidence at the plain's end wall causes a CCW rotating eddy, which in turn triggers a CW rotating eddy near the slope (Figure 5). By reducing the length of the plain to 22.5 cm in SP-Part, we eliminated the possibility of two eddies with a width-to-height ratio of about one. If subsidence caused the eddy motion, the only eddy over the plain in SP-Part would be CCW rotating. By contrast, our observations show a CW rotating eddy (Figure 9). The causal chain is therefore: the upslope flow causes a CW rotating eddy, which in turn causes strongly rising motion at the valley center for a short plain or a second (CCW rotating) eddy closer to the valley center for a longer plain. In the latter case, the CCW rotating eddy causes the familiar subsidence near the valley center. The parameter settings suggest that valleys with an aspect ratio of valley bottom width to ridge height of $2 \times 22.5 \text{ cm} : 14.9 \text{ cm} \approx 3:1$ exhibit strong rising motion over the valley center.

[37] Colette *et al.* [2003] observed layering, similar to ours, in their LES of two-dimensional valleys between mountain ranges of triangular cross section. This layering, however, could also have been the result of the initial

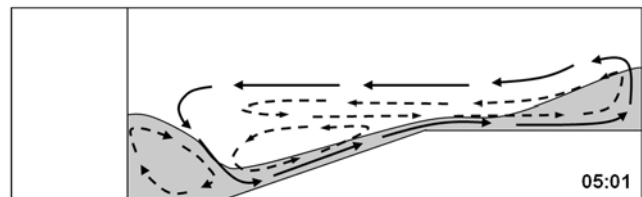


Figure 9. Rising motion over a valley center. In particle experiment SP-Part, conditions were identical to those in WT-Dye and WT-Part (Table 1) with the exception of an end wall inserted over the plain 22.5 cm from the slope (vertical line). Flow characteristics are sketched with dashed arrows (small circulations) and solid arrows (large superimposed circulation), determined from two-dimensional velocity fields. The grey region outlines the BBL.

background at the beginning of positive heat flux: a stable surface layer topped by a neutral residual layer and a stable free atmosphere. The authors ran experiments over a wide range of aspect ratios of valley bottom width to ridge height. Flow fields for a very narrow valley exhibit subsidence over the valley centre as expected. We speculate that rising motion would occur at an aspect ratio of 3:1. The closest to this ratio in the work of *Colette et al.* [2003] is a case with an aspect ratio of 2:1. The authors did not show flow fields for this case so that vertical motion cannot be directly confirmed. However, they demonstrated that in this case no inversion breakup from above occurred, implying a lack of subsidence. A possible explanation is that this is a transitional case between strong subsidence in a valley of an aspect ratio smaller than 2:1 and divergence in a valley with an aspect ratio of roughly 3:1.

[38] Future research should test how accurately the aspect ratio needs to be achieved to observe the rising motion and compare tank with field observations. The aspect ratio may be different for the atmosphere, where the CW rotating eddy may occur further from the slope (see below). Furthermore, past field measurements may not have been taken at the location of the CW rotating eddy. Unless rising motion led to condensation, it would be unnoticed. Finally, spatially inhomogeneous sensible surface heat flux and imperfect valley symmetry in the atmosphere may reduce the likelihood of strong rising motion.

[39] *Atkinson and Shahub's* [1994] three-dimensional nonhydrostatic numerical model runs covered a wide range of background stabilities and valley shapes. They observed flow regime changes at background stabilities roughly an order of magnitude smaller than stabilities in the field observations in the work of *Reuten et al.* [2005] that correspond to those in our tank experiments. For very weak stabilities, they observed strong upward motion over the valley center. We cannot draw direct comparisons with our steep slope angles, but the study by *Atkinson and Shahub* [1994] clearly demonstrates the wide range of flow characteristics possible even in a simple valley cross section.

[40] *Rampanelli et al.* [2004] ran a numerical mesoscale model with two different two-dimensional topographies, both similar to our conditions in the tank. In neither case did the model produce a CW rotating eddy. In one topography the valley side walls were 1 km high with a maximum slope angle of 15° , and the valley bottom was 1 km wide. The aspect ratio of 1:1 was probably too small to support rotating eddies over the valley bottom. In the second topography, a very long plain and plateau were connected via a slope of 3.6° , much less than our 19° . We will next look into the possible reasons for the existence of the CW rotating eddy and discuss the consequences for similarity between water tank and atmosphere.

3.3. Backscatter Boundary Layer Bulge and Depression Near the Slope Base

[41] Lidar observations at the Minnehada Park field site covering the entire morning of 25 July [*Reuten et al.*, 2005, Figure 6] did not show a BBL bulge and adjacent depression. In the atmosphere without lateral boundaries even very light crosswinds can advect aerosols laterally into the depression. Furthermore, as we will report elsewhere, upslope flows in the atmosphere under the conditions at

Minnehada Park are faster than those in the water tank; while that does not affect the overall qualitative agreement between field and tank observations, atmospheric aerosols within the upslope flow circulation return faster than the dye in the water tank and therefore mask the BBL depression. On a larger scale, this masking takes more time and the BBL depression can be observed more easily. *de Wekker* [2002] observed a BBL bulge and depression adjacent to the entire mountain range north of the Lower Fraser Valley, with a ridge height exceeding 1500 m, about twice the ridge height at Minnehada Park [*de Wekker*, 2002, Figure 3.1]. Longer distances imply longer timescales and partially explain *de Wekker's* observation that the BBL depression strengthened with time. *De Wekker* modeled the BBL depression with RAMS, but the 1-km horizontal resolution was possibly insufficient to resolve the CW eddy motion over the plain. *De Wekker* concluded that the BBL depression is associated with increased heating within and above the TBL at the slope base due to advection of warm air by the upslope flow system. Moreover, he hypothesized that subsidence over the BBL depression is enhanced by horizontal wind divergence due to upslope flow acceleration at the slope base. *Mitsumoto* [1989] speculated that the CW rotating eddy was “energetically economic.” We now combine these arguments with the water tank observations.

[42] Without compensating upslope flow, a horizontal specific-volume gradient would develop along the slope (Figure 10a). The upslope flow advects fluid of low specific volume upwards along the slope into regions of higher specific volume, thereby constantly reducing specific volume and inhibiting TBL growth in these regions. In contrast, advection over the plain does not cause cooling, and the TBL grows faster there than over the slope. At 05:01 in WT-Dye, the TBL depth h over the plain is approximately equal to the ridge height H , and to first approximation this leads to a TBL depth decreasing linearly from H to 0 along the slope (Figure 10b). Over the slope, however, a circulation appears superimposed on top of the inflow as sketched in Figure 8a. The upper branch of the circulation causes subsidence W over the lower half of the slope (Figure 10c). Following *Mitsumoto* [1989], we speculate that indeed the development of a small circulation over the slope is energetically beneficial. The CCW rotating upslope flow circulation causes a downward drag at its left border favoring the adjacent CW rotating eddy over the plain (Figure 8a). It remains open for future research why the four smaller circulations in Figure 8a are embedded in a larger circulation, although closed slope flow and plain-plateau flow circulations without the large circulation could balance mass transport.

3.4. Inhomogeneous Heating

[43] In the last two sections, we presented tank observations about a persistent CW rotating eddy over the plain adjacent to the slope, which was also observed by *Mitsumoto* [1989]. In contrast, *Chen et al.* [1996] did not observe the eddy over the plain, although their experiments, like those by *Mitsumoto* [1989], used a triangular ridge and approximately sinusoidal cycles of diurnal heating and cooling. *Chen et al.* [1996] injected hot water underneath the ridge top, from where it flowed outward toward the end walls underneath the tank bottom. Strong venting over the ridge in the experiments

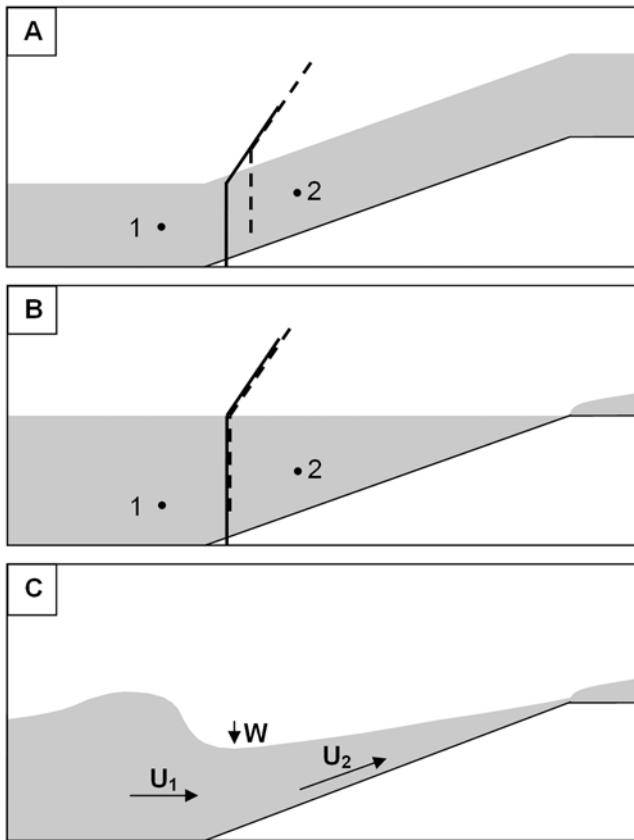


Figure 10. Schemata of TBL (gray areas), specific volume, and flows in the water tank. (a) Without compensating upslope flows, TBL depth is homogeneous. Vertical specific volume profiles for an encroachment model are sketched for point 1 (solid line) and point 2 (dashed line). A pressure gradient exists between points 1 and 2. (b) If the TBL top was horizontal, here shown for the case when TBL depth equals ridge height, specific volume profiles over plain and slope would be identical, shown for points 1 and 2. (c) TBL and flows as observed in the tank: mean inflow U_1 into the upslope flow system near point 1, mean horizontal velocity U_2 in the upslope flow layer near point 2, and mean subsidence velocity W between points 1 and 2.

of *Chen et al.* [1996] provides evidence that there was a strong heat flux increase from end wall to ridge top. By contrast, *Mitsumoto* [1989] ensured homogeneous heat flux by individually controlling the water temperature from injection pipes underneath the slope. Therefore we hypothesize that the positive heat flux gradient from left end wall to ridge top in the experiments of *Chen et al.* [1996], which was not present in the experiments of *Mitsumoto* [1989] and our whole-tank experiments, eliminates the CW rotating eddy.

[44] To test this hypothesis, we ran experiment TR-Part (Table 1), in which heat flux increased by a factor of 2.5 from the plain's end wall to the removable end wall at the ridge top (Figure 11). Because the plateau was cut off from the rest of the tank with a removable end wall, there was no plain-plateau flow. The heat flux gradient triggered long CCW rotating circulations over plain and slope (dashed

arrows) and increased the strength of the upslope flow, causing overshooting over the ridge top. One would expect that the two circulations would merge, but they remained separated by a high arch within the large circulation (solid arrows). We can therefore reject the hypothesis that the heat flux gradient in the work of *Chen et al.* [1996] destroyed the CCW rotating circulation.

[45] The evidence suggests that the CCW rotating eddy was also present in the experiments by *Chen et al.* [1996], who reported the large circulation but not the individual CCW rotating circulations and the arch between them. We speculate that the authors did not report a CCW rotating eddy because their experiments were configured to investigate large-scale motions: a 74 cm wide interrogation window and particle streak photographs taken every 30 s provided less spatial and temporal resolution than our experiments.

4. Discussion

[46] Field observations reported by *Reuten et al.* [2005] raise a number of key questions: Does the boundary layer over a heated slope coincide with the TBL over flat terrain or does it have a more complicated structure? How do upslope and return flow relate to the boundary layer structure? What are the determining parameters for venting versus recirculation of air pollutants over heated mountain slopes? We will suggest answers to these questions in the following discussion.

4.1. Comparison of Field and Tank Observations

[47] The explanation of BBL bulge and depression and CW rotating eddy over the plain near the slope base holds for atmosphere and water tank (section 4.3). A comparison of water tank images with lidar scans roughly at the time of similarity (05:01 and 1100 PST 25 July 2001, respectively) shows good qualitative agreement (Figure 12). Two minor differences are caused by greater upslope flow velocities in the atmosphere than in the tank. First, overshooting over the

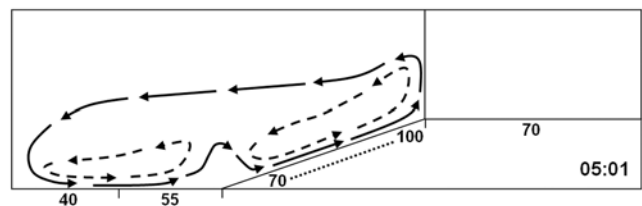


Figure 11. Flow characteristics for inhomogeneous heat flux in experiment TR-Part. This experiment was designed to reproduce qualitatively tank observations by *Chen et al.* [1996], with their time of maximum heating corresponding roughly to 05:01 in this experiment. Distribution of heat flux underneath the tank bottom is indicated by the numbers, which are in percentage of the maximum value of $0.0037 \text{ K m s}^{-1}$ right below the ridge top. Heat flux through the tank bottom was 40% for heaters 1–5, 55% for heaters 6–11, and increased in 12 increments from 70 to 100% for heaters 12–23 (Figure 1). The plateau was separated from the rest of the tank by a removable end wall (vertical line). Under the plateau, 70% of the maximum heat flux was supplied to minimize the pressure gradient across the separating wall. The arrows represent the circulations at 05:01.

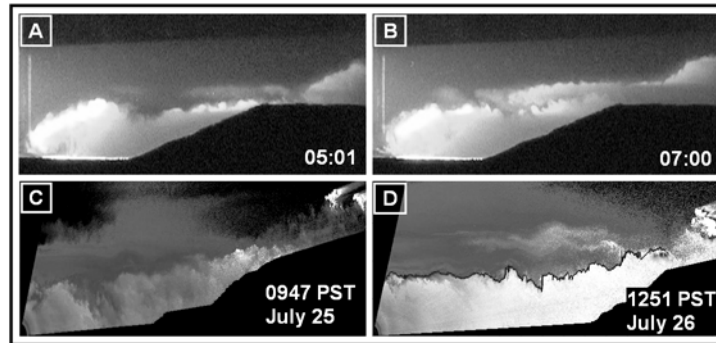


Figure 12. Comparison of WT-Dye at (a) 05:01 and (b) 07:00 with atmospheric lidar RHI scans at (c) 0947 PST 25 July 2001 and (d) 1251 PST 26 July 2001. Figures 12a and 12c show almost the entire tank width (1.3 m) and a height of about 0.3 m. Figures 12c and 12d show a width of about 8000 m and a height of about 1500 m. Lighter colors roughly represent higher dye/aerosol concentrations. The fluorescent dye in Figures 12a and 12b is illuminated from the left, where dye concentrations are exaggerated. The bright areas on the right top in Figures 12c and 12d are caused by cumulus clouds. The dark line in Figure 12d marks the BBL top. Horizontal and vertical scales of the lidar scans are adjusted to agree approximately with the scales represented by the water tank. In Figure 12d, the topography looks different from Figure 12c because the azimuth angles of the two lidar scans differed by 5° . Images in Figures 12c and 12d are adapted from *Reuten et al.* [2005, Figures 15 and 5].

ridge top is stronger in the atmosphere, well documented by cumulus clouds on the lidar scans (Figures 12c and 12d). Second, the laminar-looking elevated aerosol layer right above the turbulent TBL at 0947 PST 25 July 2001 had propagated farther over the plain than the counterpart in the water tank (Figure 12a).

[48] On 26 July, background stratification was stronger than on 25 July. At 1251 PST (Figure 12d), the BBL was approximately as deep as on the previous day at 0947 PST (Figure 12c), in good agreement with WT-Dye at 07:00 (Figure 12b).

[49] In conclusion, flow characteristics in the water tank are a good qualitative representation of atmospheric flows at Minnehada Park during the morning. Atmospheric upslope flows in the afternoon are substantially affected by sea breeze and up-valley flow, which will not be discussed here.

4.2. Atmospheric Boundary Layer Over Complex Terrain

[50] In this work, TBL depth was determined from vertical profiles of specific volume in the tank and potential temperature in the atmosphere using the parcel method; the BBL was determined from images of dye concentrations in the tank and lidar aerosol backscatter scans in the atmosphere. To clarify terminology, we distinguish the atmospheric boundary layer (ABL) from TBL and BBL. It is common to “define the boundary layer as the part of the troposphere that is directly influenced by the presence of the earth’s surface, and responds to surface forcings with a timescale of about an hour or less” [Stull, 1988]. *Seibert et al.* [2000] pointed out that this definition might require modification in complex terrain. The requirement of such fast response is often tacitly abandoned, even over flat terrain, for example in the case of the residual layer above a strongly stratified nocturnal boundary layer in the winter. A sense of continuity of entrainment zone and capping inversion from one day to the next [Stull, 1988, Figure 1.7]

suggests considering the ABL as the part of the troposphere that exchanges temperature, tracers, or moisture with the Earth’s surface within one diurnal heating cycle. Conceptually, this definition solves a key problem over complex terrain: Venting of upslope flows over mountain ridges is very fast and within one hour can create elevated aerosol-rich layers. These should therefore be considered part of the ABL, although they may remain above the entrainment zone for the entire day and therefore be counter to our intuitive understanding of the ABL. On the other hand, elevated layers (EL) that merge with the TBL within one diurnal heating cycle should be considered part of the ABL even if the merging occurs several hours later. This definition of the ABL comprises all layers that exchange air with the surface during the day. Together with inflow and outflow by advection and venting, the ABL constitutes the local atmospheric environment for the assessment of air quality in complex terrain during a diurnal cycle.

4.3. Multiscale Layering and the Relation of Upslope and Return Flow to the Boundary Layer Structure

[51] In the work of *Reuten et al.* [2005, Figure 7], field observations several kilometers from the slope suggested that TBL and BBL were identical on the mornings of 25 and 26 July 2001, when larger-scale flows were negligible. This is probably not representative for TBL and BBL directly over the slope. *de Wekker* [2002] drew a comprehensive conceptual picture of the ABL characteristics over complex terrain and clearly demonstrated that the BBL often substantially exceeds the TBL, in particular in the afternoon. Many of the complicated ABL features investigated by *de Wekker* [2002] are probably caused by “multiscale layering,” a repetition of layering processes and regime changes at increasingly larger spatial and temporal scales, which are revealed in the water tank experiments.

[52] The fastest of these processes is convection, which creates the TBL. Without horizontal inhomogeneities, no

other process could lead to further ABL structures. Short steep slopes like the one at Minnekhada Park, which was modeled by the tank experiments, drive upslope flows of several meters per second and force a compensating return flow over horizontal distances of only a few kilometers. In less than 1 hour aerosols transported from near the surface up the slope return in an EL above the TBL. The tank experiments show that ELs tend to have intermediate characteristics: aerosol concentrations and stability between those in TBL and free atmosphere (Figure 7). The underlying TBL needs less surface heating to grow into a weakly stratified EL than into the strongly stratified free atmosphere. In WT-Part, the TBL began merging with the EL at about 07:00, a typical atmospheric early afternoon case (Table 3). In the atmosphere, by comparison, the difference in aerosol concentrations between TBL and EL is a complicated function of the day's history of emissions, advection, and entrainment. Before the merging of TBL and EL, their aerosol concentrations may become indistinguishable. This may be the reason why both layers appear as one deep BBL in the field observations.

[53] *Reuten et al.* [2005] speculated in their hypothesis 3 that BBL and TBL were different for extended periods during the field observations. This is supported by the tank experiments, in which the upslope flow layer agreed with the TBL and the return flow layer with the EL at all times; together building up a BBL deeper than the underlying TBL. In the lidar scans at Minnekhada Park, the TBL and the EL within the BBL were probably indistinguishable.

[54] We argued that the large BBL depressions investigated by *de Wekker* [2002] were caused by the same kinematics as in the water tank but at a scale that is similar to the Northshore Mountains as a whole rather than the smaller individual slope at Minnekhada Park. The Northshore Mountains are approximately 100 km wide and reach an elevation of 1500–2000 m. The slope at Minnekhada Park in a tributary valley of the Northshore Mountains is only a few kilometers wide and 760 m high. In the water tank, multiscale layering is repetitive in time. All tank experiments with a heated plateau caused a plain-plateau flow circulation that removed dye-rich fluid from the upslope flow circulation at the slope top and returned it above the plain in the return flow part of the plain-plateau circulation. Upslope and plain-plateau flow circulation merged at approximately the same time as the TBL merged with the EL. At this point, the process of developing an EL above the TBL was repeated at the larger scale of the combined upslope plain-plateau flow circulation. Eventually the TBL merged with the new EL before 13:00, which is similar to typical atmospheric settings just before the time of maximum heating (Table 3). By 13:00, the TBL had grown beyond the scale of the underlying topography, which could not provide further horizontal inhomogeneities to continue the multiscale layering.

[55] In many real atmospheric settings, horizontal inhomogeneities are likely to continue at increasingly larger scales, and multiscale layering is only limited by the finite duration of the diurnal heating cycle or the depth of nearby topography. Furthermore, inhomogeneities often occur at more closely spaced scales and are not restricted to upslope flows but may include along- and cross-valley flows, topographically altered synoptic winds, and flows caused

by land-use variations. Such closely spaced discrete scales cause a de facto “continuum in topographic complexity and scale” [*Whiteman*, 1990]. A water tank of sufficiently simple topography can clearly discriminate the steps in the multiscale layering, which may be practically indistinguishable in the atmosphere.

[56] *Rampanelli and Zardi* [2004] developed a method of fitting a piecewise smoothly connected curve to the well-mixed and entrainment layers of the ABL and applied the method to measurements in complex terrain surrounding the Trento region, Italy. Several examples show entrainment layers much deeper than the underlying well-mixed layer. A close look at the measured profiles suggests that the authors may have observed several-hundred meter deep ELs, which were fitted within the entrainment layer. It may be worthwhile investigating these data sets further by trying to fit multiple layers with the method suggested by *Rampanelli and Zardi* [2004]. Bayesian model comparison could be used to decide if enough evidence is present in the data to justify fitting of additional layers [e.g., *Gregory*, 2005].

4.4. Venting Versus Trapping of Air Pollutants

[57] The water tank is an extreme simplification of the complexity of the real atmosphere. This even holds for nearly ideal conditions at Minnekhada Park during the morning of 25 July 2001. Nevertheless, the detailed investigations of the flows in the water tank permit conclusions about atmospheric flows under typically less ideal conditions. Essentially, local trapping of air pollution over heated mountain slopes occurs when an EL resides over a growing TBL long enough to be entrained. The scenarios that typically, albeit not always, support this, are now briefly discussed.

[58] Weaker larger-scale flows lengthen the residence time of the EL over the TBL and therefore increase the chance of entrainment.

[59] Stronger sensible surface heat flux supports the entrainment of the EL by a deeper TBL. This effect is partly offset by an increased volume into which air pollutants are dispersed and by a stronger upslope flow potentially leading to a higher EL, which decreases the chance of entrainment.

[60] Similarly, weaker stratification supports the entrainment of the EL by a deeper TBL. This effect could partly be offset by the increased volume into which air pollutants are dispersed. Furthermore, the impact of background stratification on upslope flow velocity is still an open question. Numerical experiments over a wide range of stratifications showed regimes where the dependence of upslope flow velocity on stratification differed substantially [*Atkinson and Shahub*, 1994]. We cannot confirm this because of large uncertainties in field observations and a very narrow range of background stratifications in the field data [*Reuten et al.*, 2005] and the water tank experiments (Table 1). The consequences of nonlinear stratification, e.g., under a capping inversion, are not discussed here.

[61] A short plateau or no plateau increases the chances for trapping compared to long plateaus, because a plain-plateau flow removes a substantial fraction of the air pollutants from the upslope flow circulation into a higher EL. In addition, for a longer plateau it takes the plain-plateau circulation longer to return the air pollutants to the

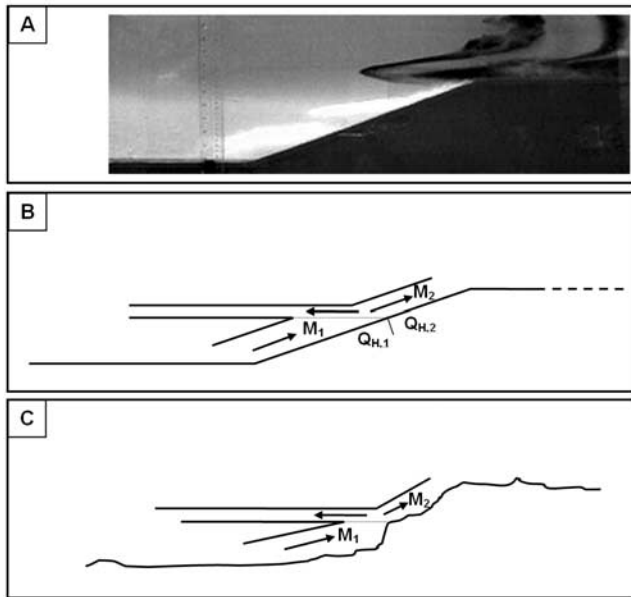


Figure 13. (a) Video frame and (b) schemata of mass flux breakup over the slope caused by a drop of surface heat flux in tank experiment HFD-Dye and (c) schemata of mass-flux breakup caused by an abrupt slope angle change above a ledge. In Figure 13a a substantial surface heat flux decrement occurred in the upper third of the slope. Part of a plume of bright dye, originally released at the slope base, has been carried upslope. At about two-third of the total slope length the flow has separated into an EL intruding into the plain region and a residual upslope flow layer. In Figure 13b, lower and upper surface heat fluxes are denoted by $Q_{H,1}$ and $Q_{H,2}$, respectively. Mass fluxes of upslope flow below the decrement and residual upslope flow above the decrement are denoted by M_1 and M_2 . C is similarly to Figure 13b; mass fluxes of upslope flow below the ledge and residual upslope flow above the ledge are denoted by M_1 and M_2 .

slope region, thereby decreasing the chance of reentraining them.

[62] Approximately symmetric geometry, like in the perfect mirror symmetry of the tank, suppresses the possibility of cross flows over the ridge or to the other side of the valley; air pollution can only escape from the surface by transport into ELs that are not reentrained during one diurnal cycle.

[63] A low ridge leads to lower EL. The smaller a mountain the more likely it will recirculate rather than vent air pollutants.

[64] *Vergeiner* [1982] hypothesized that sensible surface heat flux inhomogeneities, e.g., a substantial drop of heat flux along the slope surface, can lead to a flow split at the inhomogeneity and therefore a low EL. We confirmed this hypothesis in tank experiment HFD-Dye (Figure 13a). Our tank design with individually controllable heaters underneath the slope could be used for future research to establish a quantitative relationship between heat flux decrements and mass balance in the split flow (Figure 13b).

[65] *Vergeiner* [1982] also hypothesized that an abrupt slope angle drop, e.g., over a ledge, can lead to a flow split similar to the case of a heat flux decrement (Figure 13c). This hypothesis is plausible but hard to test with our tank.

[66] Finally, research should be carried out in the future to investigate if abrupt surface roughness changes also lead to a flow split.

5. Conclusions

[67] We showed observations from a bottom-heated salt-stratified water tank with a 19° slope and adjacent plain and plateau. Early in the experiments, these agree qualitatively with field observations at an approximately homogeneous 19° slope in Minnehada Park, British Columbia, Canada. Later, three-dimensional flow characteristics in the tank and sea breeze and valley flows in the atmosphere may limit similarity.

[68] Over the slope, advection of fluid with lower specific volume leads to a shallow thermal boundary layer (TBL), causing in turn a clockwise rotating eddy over the plain near the slope. The full tank models the flow in a valley with a valley bottom to ridge height ratio of 6:1. For this aspect ratio, a counter clockwise rotating eddy near the valley center creates subsidence over the valley center. When the aspect ratio is reduced to 3:1, the counter clockwise rotating eddy is suppressed and strongly rising motion occurs instead.

[69] Slope and plateau cause horizontal temperature inhomogeneities, which lead to elevated layers (EL) above the TBL. The ELs have stability and dye/aerosol concentrations intermediate between TBL and background. An EL is entrained into the TBL if sufficient heating continues. Before the entrainment, the backscatter of EL and TBL can be indistinguishable, so that EL and TBL form one deep backscatter boundary layer. The entrainment occurs rapidly as a flow regime change. In the experiments, the upslope flow layer agrees with the TBL and the return flow layer with the EL.

[70] We suggested defining the ABL as comprising all layers that are in contact with surface forcings during one diurnal cycle. In particular, this definition includes polluted ELs that are entrained into the growing TBL after more than the commonly used 1-hour timescale. In this case, pollutants are effectively trapped.

[71] The tank experiments hint at the conditions that are typically conducive to air pollutant trapping: weaker larger-scale flows, stronger sensible surface heat flux, weaker stratification, a short plateau or no plateau, approximately symmetric geometry, a low ridge, and inhomogeneities in sensible surface heat flux. We also speculate that inhomogeneities in slope angle and surface roughness can enhance trapping. The complexity of real-world topography will typically lead to layering, venting, and trapping in a near continuum of multiple scales.

Appendix A

[72] In water tanks with a flat horizontal bottom, a linear stratification can be achieved with the two-bucket method [*Fortuin*, 1960]. We describe here the modifications we made to that method to account for the slope in the tank.

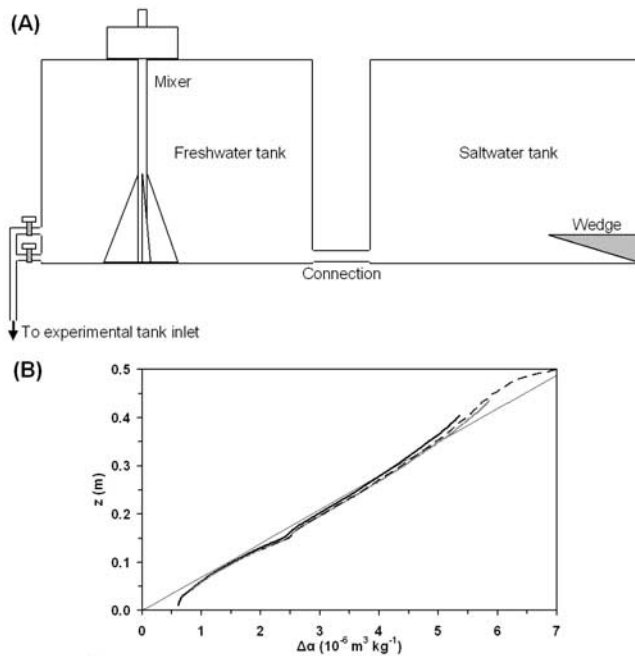


Figure A1. (a) Schematic side view of the filling tank setup and (b) typical initial specific volume profiles. In Figure A1a the mixer is inside the freshwater tank reaching close to the bottom. The solid wedge fills the entire width of the saltwater tank. Both tanks are connected via a hose on the bottom. The “experimental tank inlet” releases the water from the freshwater tank at the bottom of the experimental tank. The top faucet stops draining when the water level in the saltwater tank reaches the top of the wedge. In Figure A1b the three vertical profiles were measured before the start of experiment SP-Part in one synchronous descent of three conductivity and temperature probes over three different locations (plain, slope near base, and slope near ridge). We made minor adjustments to match the profiles near the tank bottom. The straight thin diagonal line shows the expected profile.

[73] The experimental tank is filled at the tank bottom through an inlet, which is fed from a freshwater tank (Figure A1a). The freshwater tank is connected at the bottom with a saltwater tank of the same dimensions so that both tanks always have the same water level during the draining process. The mixer in the freshwater tank mixes the water in the freshwater tank with the saltier water supplied through the connection. During the filling process, the salt concentration in the experimental tank increases pushing previous layers of fresher, and therefore less dense, water up. Therefore the experimental tank is filled from top to bottom. The first drainage step through the upper faucet terminates when the water level in the saltwater tank reaches the top of the solid wedge. A small amount of salt is dissolved in the saltwater tank before continuing the filling process through the bottom faucet. The wedge in the saltwater tank modifies the volume of saltwater supplied to the freshwater tank and compensates for the changing volume in the bottom 14.9 cm of the experimental tank. We determined the dimensions of the wedge and the amount of salt needed initially and between the first and second drainage step in a spreadsheet

application. Figure A1b shows the specific-volume profiles at three different locations before the start of one of the experiments described below. The volume compensation at the height of the plateau (14.9 cm) is visible only as a small wiggle in all three profiles, but the agreement with the expected profile is good. Because of technical problems with our filling tanks, we cannot avoid the weaker stratification in the bottom 3 cm. However, since the boundary layer grows much deeper than 3 cm early in the experiments the weaker stratification does not seem to affect the experiments substantially.

List of Frequently Used Acronyms

ABL	Atmospheric Boundary Layer
BBL	Backscatter Boundary Layer
CCW	Counter Clockwise
CW	Clockwise
EL	Elevated Layer
HFD-Dye	Dye experiment with a Heat Flux Decrement about two-thirds up the slope
LES	Large-Eddy Simulation
PST	Pacific Standard Time (UTC-0800 h)
SP-Part	Particle experiment using a Shortened Plain
TBL	Thermal Boundary Layer
TR-Part	Particle experiment using a Triangular Ridge (end-wall at top of slope)
WT-Dye	Dye experiment using the Whole Tank
WT-Part	Particle experiment using the Whole Tank

[74] **Acknowledgments.** We gratefully acknowledge the support in the Department of Civil Engineering at UBC: Greg Lawrence for providing laboratory space for the water tank and sharing computer resources and instrumentation; Bill Leung, Scott Jackson, and Harald Schrempf for their contributions to designing and building the tank. We thank Ian Chan for his help on tank redesign, MatPIV, and several experiments. Funding support was provided by grants from NSERC and CFCAS to Douw Steyn and Susan Allen.

References

- Atkinson, B. W. (1981), *Meso-Scale Atmospheric Circulations*, 495 pp., Elsevier, New York.
- Atkinson, B. W., and A. N. Shahub (1994), Orographic and stability effects on day-time, valley-side slope flows, *Boundary Layer Meteorol.*, *68*, 275–300.
- Banta, R. M. (1984), Daytime boundary layer evolution over mountainous terrain. Part 1: Observations of the dry circulations, *Mon. Weather Rev.*, *112*, 340–356.
- Blumen, W., (Ed.) (1990), *Atmospheric Processes Over Complex Terrain*, 323 pp., *Meteorol. Monogr.* 23, Am. Meteorol. Soc., Boston, Mass.
- Brehm, M. (1986), Experimentelle und numerische Untersuchungen der Hangwindschicht und ihre Rolle bei der Erwärmung von Tälern, Ph.D. thesis, 150 pp., Ludwig-Maximilian-Univ., München, Germany.
- Buckingham, E. (1914), On physically similar systems; illustrations of the use of dimensional equations, *Phys. Rev. Lett., Second Series, IV*, 345–376.
- Carson, D. J. (1973), The development of a dry inversion-capped convectively unstable boundary layer, *Q. J. R. Meteorol. Soc.*, *99*, 450–467.
- Chen, R.-R., N. S. Berman, D. L. Boyer, and H. J. S. Fernando (1996), Physical model of diurnal heating in the vicinity of a two-dimensional ridge, *J. Atmos. Sci.*, *53*, 62–85.
- Chow, F. K., A. P. Weigel, R. L. Street, M. W. Rotach, and M. Xue (2006), High-resolution large-eddy simulations of flow in a steep alpine valley. Part I: Methodology, verification and sensitivity studies, *J. Appl. Meteorol. Climatol.*, *45*, 63–86.
- Colette, A., F. K. Chow, and R. L. Street (2003), A numerical study of inversion-layer breakup and the effects of topographic shading in idealized valleys, *J. Appl. Meteorol.*, *42*, 1255–1272.
- Deardorff, J. W., and G. E. Willis (1987), Turbulence within a baroclinic laboratory mixed layer above a sloping surface, *J. Atmos. Sci.*, *44*, 772–778.

- de Wekker, S. F. J. (2002), Structure and morphology of the convective boundary layer in mountainous terrain, Ph.D. thesis, 191 pp., Dep. of Earth and Ocean Sci., Univ. of Brit. Columbia, Vancouver, B.C., Canada.
- de Wekker, S. F. J., D. G. Steyn, J. D. Fast, M. W. Rotach, and S. Zhong (2005), The performance of RAMS in representing the convective boundary layer structure in a very steep valley, *Environ. Fluid Mech.*, 5, 35–62.
- Eck, S., M. S. Kharicha, A. Ishmurzin, and A. Ludwig (2005), Measurement and simulation of temperature and velocity fields during the cooling of water in a die casting model, *Mater. Sci. Eng. A*, 413, 79–84.
- Egger, J. (1981), On the linear two-dimensional theory of thermally induced slope winds, *Beitr. Phys. Freien Atmos.*, 54, 465–481.
- Fortuin, J. (1960), Theory and application of two supplementary methods of constructing density gradient columns, *J. Polymer Sci.*, XLIV, 505–515.
- Gregory, P. (2005), *Bayesian Logical Data Analysis for the Physical Sciences*, 488 pp., Cambridge Univ. Press, New York.
- Grønås, S., and A. D. Sandvik (1999), Numerical simulations of local winds over steep orography in the storm over North Norway on October 12, 1996, *J. Geophys. Res.*, 104, 9107–9120.
- Haiden, T. (1990), Analytische Untersuchungen zur konvektiven Grenzschicht im Gebirge, Ph.D. thesis, 140 pp., Univ. Wien, Austria.
- Haiden, T. (2003), On the pressure field in the slope wind layer, *J. Atmos. Sci.*, 60, 1632–1635.
- Hunt, J. C. R., H. J. S. Fernando, and M. Princevac (2003), Unsteady thermally driven flows on gentle slopes, *J. Atmos. Sci.*, 60, 2169–2182.
- Ingel', L. K. (2000), Nonlinear theory of slope flows, *Izv. Russ. Acad. Sci. Atmos. Oceanic Phys.*, 36, 384–389.
- Kondo, H. (1984), The difference of the slope wind between day and night, *J. Meteorol. Soc. Jpn.*, 62, 224–232.
- Kuwagata, T., and J. Kondo (1989), Observations and modeling of thermally induced upslope flows, *Boundary Layer Meteorol.*, 49, 265–293.
- Mitsumoto, S. (1989), A laboratory experiment on the slope wind, *J. Meteorol. Soc. Jpn.*, 67, 565–574.
- Moroni, M., and A. Cenedese (2006), Penetrative convection in stratified fluids: Velocity and temperature measurements, *Nonlinear Processes Geophys.*, 13, 353–363.
- Petkovšek, Z. (1982), Ein einfaches Modell des Tages-Hangwindes, *Z. Meteorol.*, 32, 31–41.
- Prandtl, L. (1952), *Essentials of Fluid Dynamics*, 452 pp., Blackie Acad. and Prof., New York.
- Rampanelli, G., and D. Zardi (2004), A method to determine the capping inversion of the convective boundary layer, *J. Appl. Meteorol.*, 43, 925–933.
- Rampanelli, G., D. Zardi, and R. Rotunno (2004), Mechanisms of up-valley winds, *J. Atmos. Sci.*, 61, 3097–3111.
- Reuten, C. (2006), Scaling and kinematics of daytime slope flow systems, Ph.D. thesis, 284 pp., Dep. of Earth and Ocean Sci., Univ. of Brit. Columbia, Vancouver, B. C., Canada.
- Reuten, C., D. G. Steyn, K. B. Strawbridge, and P. Bovis (2005), Observations of the relation between upslope flows and the convective boundary layer in steep terrain, *Boundary Layer Meteorol.*, 116, 37–61.
- Revell, M. J., D. Purnell, and M. K. Lauren (1996), Requirements for large-eddy simulation of surface wind gusts in a mountain valley, *Boundary Layer Meteorol.*, 80, 333–353.
- Schumann, U. (1990), Large-eddy simulation of the upslope boundary layer, *Q. J. R. Meteorol. Soc.*, 116, 637–670.
- Segal, M., Y. Ookouchi, and R. A. Pielke (1987), On the effect of steep slope orientation on the intensity of daytime upslope flow, *J. Atmos. Sci.*, 44, 3587–3592.
- Seibert, P., F. Beyrich, S.-E. Gryning, S. Joffre, A. Rasmussen, and P. Tercier (2000), Review and intercomparison of operational methods for the determination of the mixing height, *Atmos. Environ.*, 34, 1001–1027.
- Strawbridge, K. B., and B. J. Snyder (2004), Planetary boundary layer height determination during Pacific 2001 using the advantage of a scanning lidar instrument, *Atmos. Environ.*, 38, 5861–5871.
- Stull, R. B. (1988), *An Introduction to Boundary Layer Meteorology*, 670 pp., Springer, New York.
- Turner, J. S. (1973) *Buoyancy Effects in Fluids*, 368 pp., Cambridge Univ. Press, New York.
- Vergeiner, I. (1982), Eine energetische Theorie der Hangwinde, paper presented at 17 Internationale Tagung Alpine Meteorologie, Berchtesgarden 1982, *Ann. Meteorol. NF*, 19, 189–191.
- Vergeiner, I., and E. Dreiseitl (1987), Valley winds and slope winds—Observations and elementary thoughts, *Meteorol. Atmos. Phys.*, 36, 264–286.
- Vogel, B., G. Adrian, and F. Fiedler (1987), *MESOKLIP-Analysen der meteorologischen Beobachtungen von mesoskaligen Phänomenen im Oberrheingraben*, 369 pp., Inst. für Meteorologie und Klimaforschung der Univ. Karlsruhe, Karlsruhe, Germany.
- Weigel, A. P., F. K. Chow, M. W. Rotach, R. L. Street, and M. Xue (2006a), High-resolution large-eddy simulations of flow in a steep alpine valley. Part II: Flow structure and heat budgets, *J. Appl. Meteorol. Climatol.*, 45, 87–107.
- Weigel, A. P., F. K. Chow, and M. W. Rotach (2006b), On the nature of turbulent kinetic energy in a steep and narrow Alpine valley, *Boundary Layer Meteorol.*, 123, 177–199.
- Whiteman, C. D. (1990), Observations of thermally developed wind systems in mountainous terrain, in *Atmospheric Processes Over Complex Terrain*, *Boston Meteorol. Monogr.*, vol. 23, edited by W. Blumen, pp. 5–42, Am. Meteorol. Soc., Boston.
- Whiteman, C. D. (2000), *Mountain Meteorology: Fundamentals and Applications*, 376 pp., Oxford Univ. Press, New York.
- Wooldridge, G. L., and E. L. McIntyre (1986), The dynamics of the planetary boundary layer over a heated mountain slope, *Geofizika*, 3, 3–21.
- Ye, Z. J., M. Segal, and R. A. Pielke (1987), Effects of atmospheric thermal stability and slope steepness on the development of daytime thermally induced upslope flow, *J. Atmos. Sci.*, 44, 3341–3354.

S. Allen, C. Reuten, and D. Steyn, Department of Earth and Ocean Sciences, University of British Columbia, 6339 Stores Road, Vancouver, BC, Canada V6T 1Z4. (creuten@eos.ubc.ca)